

# Flexible Compact High-Order FD-FD Algorithm for Computing Mode Fields of Microwave Waveguides with Regular and Reentrant Corners

Sin-Yuan Mu and Hung-Wen Chang\*

**Abstract**—We present a highly accurate frequency-domain finite-difference algorithm for computing mode field solutions of microwave waveguides with regular and reentrant corners. Based on FBS (Fourier-Bessel series)-derived 3-by-3 compact coefficients, our method allows for a flexible layout of the 2-D uniform grids so that distance from the waveguide boundaries to the adjacent unknowns can be arbitrary. Fourth to sixth-order convergent rates of the proposed coefficients are verified by resonance-frequency error analysis for rectangular microwave waveguides for both TE/TM polarizations. We also study the first four Neumann/Dirichlet eigenvalues of the L-shaped MW-WGs calculated by the flexible scheme, and the Neumann results are reported for the first time. Although our results achieve sixth-order accuracy for analytic modes, the order of accuracy is about one and a third for both fundamental TE and TM modes due to singularity around the reentrant corner.

## 1. INTRODUCTION

In the past seventy years, researchers had tried various specific techniques to increase the numerical accuracy for modeling a physical waveguide structure with sharp boundary corners, such as H-shaped waveguides, L-shaped waveguides, and waveguides with fin line like a metal knife. Tracing the history, the concept of particular treatment for domain around those corners can be dated back to Motz's work in 1947 [1]. Motz applied circular harmonics (like-FBS) expansion to obtain better finite-difference (FD) coefficients near the vertices of a reentrant corner and those of a metal knife edge. Around these points, mild and strong singularities occur. Such electromagnetic (EM) fields are related to meromorphic functions [2, 3]. It is strange that most researches focused just on vertices of PEC wedges and had missed possible improvement over the classical 5-point and 9-point FD coefficients for Helmholtz equation in uniform region. In authors' own view, there are two possible reasons for this. On one hand, conventional frequency-domain finite-difference (FD-FD) methods cannot handle structures with complex geometry, so more people worked on finite element method (FEM) to better treat arbitrary PEC boundaries. On the other hand, finite-difference time-domain (FD-TD) algorithms, unlike FD-FD methods, without having to invert huge sparse matrices, had enjoyed much popularity for complex and large physical problems. As the memory size gets larger and the CPU became faster in the late twentieth century, frequency-domain methods become plausible as they are better suited for high-Q structures and for those frequency-domain phenomena. It was until Hadley's work (2002) [4] (and independently by Chang and Mu (2010) [5]) that FBS-based technique for grids inside a 2-D uniform region were available. Hadley also derived coefficients for points near dielectric interface, and even for points near dielectric corner through tedious algebraic manipulation [6]. However, rates of convergence for Hadley's numerical modal indices were less than he had expected, and the reasons were not given in his papers. We will discuss this

---

*Received 18 February 2019, Accepted 24 April 2019, Scheduled 27 April 2019*

\* Corresponding author: Hung-Wen Chang (hchang@mail.nsysu.edu.tw).

The authors are with the Department of Photonics, National Sun Yat-sen University, Kaohsiung 80424, Taiwan, R.O.C.

point in detail in subsequent paragraphs. The remedy for solving problems with Dirichlet/Neumann singular boundary by FD-FD and FEM has been proposed by Magura et al. (2017) [7], but it requires much additional computational effort to subtract the singular field from the whole modal fields.

In this paper we take a deep look into the FD-FD method for analyzing microwave waveguide (MW-WG) with regular and reentrant corners made of perfect electric conductors (PEC). Fig. 1 shows an H-shaped MW-WG with the FD-FD grid layout where the FD-mesh lines are represented by dashed lines. EM fields are sampled on mesh line intersections. Some mesh lines meet with the PEC boundary, but others may not. For example, when the width to height ratio of a rectangular MW-WG is not an integral ratio, the bordering field points are not located exactly on or half-a-grid spacing from the PEC boundary. Hence we need high-order customized FD coefficients for these special nodes near boundary edges and corners. Otherwise, it will lead to less accurate simulation results. Four types of such 3-by-3 stencils are also shown in Fig. 1. All FD formulations in this paper adopt the variable order illustrated in the right part of Fig. 1. We will systematically discuss effects of mesh offsets (distance of border grids from the nearby PEC walls) on the simulation accuracy. Our goals are to maintain, under the compact-coefficient framework, high-order accuracy in discretizing Helmholtz equation for both interior grids and those near PEC boundaries with a flexible grid layout.

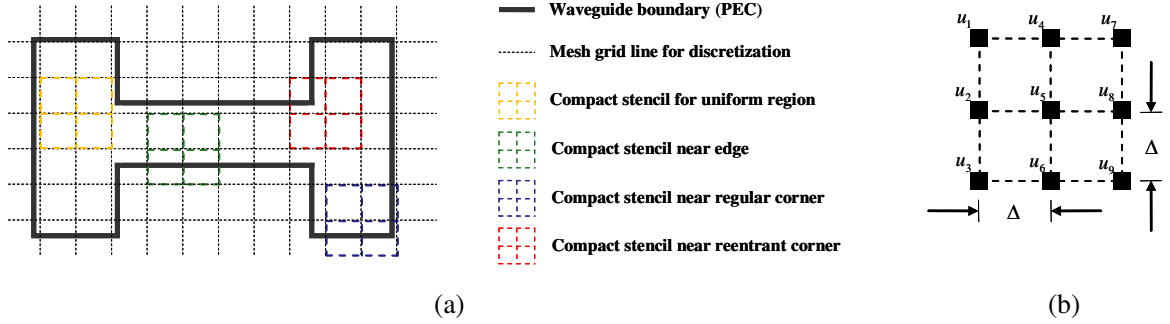


**Figure 1.** (a) FD-FD mesh layout for an H-shaped MW-WG. (b) A compact 3-by-3, 9-point stencil with numbered nodal fields is given. The grid size for the uniform stencil is  $\Delta$ .

We will discuss our proposed FBSE-based flexible compact coefficients in FD-FD methods for points near boundary edges, regular corners, and reentrant corners. The effectiveness of the proposed coefficients is verified by local field error analysis and TE/TM modal index computation of a rectangular MW-WG. And for the reentrant corner, it is verified by examining first four Dirichlet/Neumann eigenvalues of an L-shaped WG. Final numerical results of our algorithm demonstrate sixth-order accuracy for analytic modes, but the order of convergence is lowered to about one and a third/two and two third for modes with mild singularity around the reentrant corner.

## 2. EM FIELDS NEAR LOCAL WEDGES

To compute mode field solutions we may choose  $H_z$  component for transverse electric (TE) modes ( $E_z \equiv 0$ ) or  $E_z$  for transverse magnetic (TM) modes ( $H_z \equiv 0$ ) [8]. Both  $H_z$  and  $E_z$  satisfy the Helmholtz equation given by Eq. (1), where  $\nabla_t^2$  is the transverse Laplacian, and  $\xi$  is the transverse wavenumber. Let the operating angular frequency be  $\omega$ , and let the mode propagation constant be  $\beta$ . Then  $\xi^2 = k^2 - \beta^2$ , where  $k = \omega\sqrt{\mu_0\epsilon}$ , with  $\epsilon$  and  $\mu_0$  being the permittivity and free-space permeability, respectively. Note that the waveguide cutoff frequency  $f_c$  is proportional to the cutoff wavenumber  $\xi$  (since  $\beta \equiv 0$ ).

$$(\nabla_t^2 + \xi^2) u = 0, \quad f_c = \frac{\xi c}{2\pi}, \quad u \equiv \begin{cases} H_z, & \text{TE} \\ E_z, & \text{TM} \end{cases}. \quad (1)$$

According to Hadley [4], Chang and Mu [5], 2-D EM field solutions in the interior uniform region

can be well approximated by a truncated Fourier-Bessel series (FBS) for both TE and TM cases.

$$u(\rho, \phi) = a_0 J_0(\xi\rho) + \sum_{m=1}^M J_m(\xi\rho) [a_m \cos(m\phi) + b_m \sin(m\phi)]. \quad (\text{FBS}) \quad (2)$$

On the surface of the perfect electric conductor (PEC) all tangential electric field components should be zero. In the mathematical setup, the scalar function  $u(\rho, \phi, z)$  representing  $H_z/E_z$  satisfies the Neumann boundary condition (NBC) for a TE case and the Dirichlet boundary condition (DBC) for a TM case. Hence, the particular solutions of Eq. (1) near a PEC wedge shown in Fig. 2 are expressed as Eqs. (3a)–(3b) [9].

$$u(\rho, \phi) = \begin{cases} a_0 J_0(\xi\rho) + \sum_{m=1}^{\infty} a_{\nu_m} f_{\nu_m}^c(\rho, \phi), & \text{TE} \\ \sum_{m=1}^{\infty} b_{\nu_m} f_{\nu_m}^s(\rho, \phi), & \text{TM} \end{cases}, \quad 0 \leq \phi \leq \theta_0. \quad (3a)$$

$$\begin{cases} f_{\nu_m}^c(\rho, \phi) = J_{\nu_m}(\xi\rho) \cos(\nu_m\phi) \\ f_{\nu_m}^s(\rho, \phi) = J_{\nu_m}(\xi\rho) \sin(\nu_m\phi) \end{cases}, \quad \nu_m = \frac{m\pi}{\theta_0}, \quad m \in \mathbb{N}. \quad (3b)$$

In Eq. (3b),  $\mathbb{N}$  indicates the set of natural numbers. Boundary conditions and asymptotic behaviors of all EM components near a PEC wedge of an MW-WG are summarized in Table 1, where all expressions are in terms of local cylindrical coordinates defined in Fig. 2. In Table 1,  $\partial_\rho u$  and  $\partial_\phi u$  represent partial derivatives of function  $u$  with respect to  $\rho$  and  $\phi$ . Note that EM field characteristics near the wedge are dominated by its included angle  $\theta_0$ . When  $\theta_0 \leq \pi$ , all EM components are continuous and finite at the vertex. However, mild singularity may still exist at that point unless  $\theta_0$  takes the form of  $\pi/n$ ,  $n \in \mathbb{N}$  [9]. For example, considering the case  $\theta_0 = 2\pi/3$ , the first TM asymptotic term of  $u(\rho, \phi)$  is proportional to  $\rho^{3/2}$ , and thus the field itself ( $E_z$ ) and its first derivative ( $E_\rho$  and  $H_\phi$ ) are continuous and finite at the vertex, but its second derivative diverges.

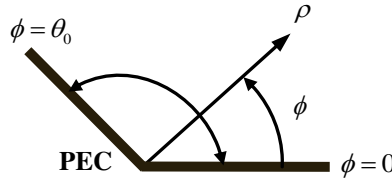


**Figure 2.** Illustration of a boundary wedge made of perfect electric conductor (PEC) with the included angle denoted by  $\theta_0$ . The cylindrical coordinate system is centered at the wedge vertex.

**Table 1.** Boundary conditions and asymptotic behaviors of EM components near a PEC wedge of a MW-WG (as shown in Fig. 2).

Transverse Components	Expressions		Asymptotic Form (as $\rho \rightarrow 0$ )	Comments on the Limit Value (as $\rho \rightarrow 0$ )	
	TE ( $u \equiv H_z, E_z \equiv 0$ )	TM ( $u \equiv E_z, H_z \equiv 0$ )		Divergent if $\theta_0 > \pi$ .	Singular when $\theta_0 \neq \pi/n, n \in \mathbb{N}$ .
$E_\phi$	$\xi^{-2} (-\bar{z} \partial_\rho u)$	$\xi^{-2} (-j\beta \rho^{-1} \partial_\phi u)$	$A \rho^{\pi/\theta_0 - 1} \cos(\pi\phi/\theta_0)$		
$H_\rho$	$\xi^{-2} (-j\beta \partial_\rho u)$	$\xi^{-2} (\bar{\sigma} \rho^{-1} \partial_\phi u)$	$B \rho^{\pi/\theta_0 - 1} \cos(\pi\phi/\theta_0)$		
$E_\rho$	$\xi^{-2} (\bar{z} \rho^{-1} \partial_\phi u)$	$\xi^{-2} (-j\beta \partial_\rho u)$	$C \rho^{\pi/\theta_0 - 1} \sin(\pi\phi/\theta_0)$		
$H_\phi$	$\xi^{-2} (-j\beta \rho^{-1} \partial_\phi u)$	$\xi^{-2} (-\bar{\sigma} \partial_\rho u)$	$D \rho^{\pi/\theta_0 - 1} \sin(\pi\phi/\theta_0)$		
B.C.s*	$E_z = 0$	Automatically satisfying	$u(\rho, \phi = 0) = 0$ $u(\rho, \phi = \theta_0) = 0$	*B.C.s: boundary conditions. *Parameter definitions: $\bar{z} \triangleq -j\omega\mu_0, \bar{\sigma} \triangleq j\omega\varepsilon$ , and thus $k^2 = \bar{z}\bar{\sigma}$ .	
	$E_\rho = 0$	$\rho^{-1} \partial_\phi u(\rho, \phi = 0) = 0$			
	$H_\phi = 0$	$\rho^{-1} \partial_\phi u(\rho, \phi = \theta_0) = 0$			

### 3. COMPACT FD-FD ALGORITHMS

Although high-order FD-FD solver may be obtained using non-compact coefficients, they lead to matrices with wider bandwidth which is undesirable due to increased storage and computational costs. A compact 9-point stencil with numbered nodal fields is shown in Fig. 2. The general expression of FD-like algebraic relation for such a stencil is given by Eq. (4), where the interested central field  $u_5$  is related to the weighted sum of the immediate surrounding nodal fields.

$$\begin{aligned} u_5 &= \sum_{m=1, m \neq 5}^9 W_m u_m = \mathbf{w} \mathbf{u}, \\ \mathbf{w} &= [ W_1 \quad W_2 \quad W_3 \quad W_4 \quad W_6 \quad W_7 \quad W_8 \quad W_9 ], \\ \mathbf{u} &= [ u_1 \quad u_2 \quad u_3 \quad u_4 \quad u_6 \quad u_7 \quad u_8 \quad u_9 ]^T. \end{aligned} \quad (4)$$

If the nodal field  $u_m$  is located outside the computation domain, the associated coefficient  $W_m$  is set to be zero. Compact 3-by-3 stencils enclosing a horizontal or a vertical boundary PEC are discussed in the subsequent sections.

#### 3.1. Coefficients for Uniform Region (UR)

Based on [4] and [5], the sixth-order accurate coefficients for uniform region are given by Eq. (5) (LFE-9). The acronym LFE represents local field expansion.

$$\begin{aligned} u_5 &= W_0^{-1} W_+ (u_2 + u_4 + u_6 + u_8) + W_0^{-1} W_\times (u_1 + u_3 + u_7 + u_9), \\ W_0 &= 4(J_0 W_+ + J_0^s W_\times), \quad W_+ = J_4^s, \quad W_\times = J_4. \end{aligned} \quad (5)$$

In Eq. (5),  $J_i = J_i(V_t)$ , and  $J_i^s = J_i(\sqrt{2}V_t)$  ( $i = 0, 4$ ), where  $V_t = \xi\Delta$ , which is the normalized transverse wavenumber.

#### 3.2. Coefficients for Boundary Edge ( $\theta_0 = \pi$ )

In Figs. 3(a)–3(d) we show four 9-point stencil grid layouts near PEC boundaries. The black squares indicate interior nodes. The green squares and blue ones indicate nodes near edges and near regular corners, respectively. The red squares indicate nodes near reentrant corners. The black crosses indicate nodes outside computation domain. The red circles are vertices of reentrant corners. The offset for the (a) case is  $d (= t\Delta)$  whereas  $d_x (= t_x\Delta)$  and  $d_y (= t_y\Delta)$  are horizontal and vertical offsets for the other three cases. When  $0 \leq t < 1$ , PEC edges alter the uniform-region coefficients for both TM and TE cases. When  $t = 0$ , the case for TM polarization is trivial, and the 4th-order accurate coefficients and the 6th-order accurate ones for Neumann boundary conditions have been proposed in Eq. (40) of [10] and in Eq. (53) of [11], respectively. Evaluating  $u_i (\triangleq (\rho_i, \phi_i), i = 1, 2, 4, 5, 7, 8)$  by Eq. (6), the truncated version of Eqs. (3a)–(3b) for the case  $\theta_0 = \pi$  leads to Eqs. (7a)–(7b) for TE modes and to Eqs. (8a)–(8b) for TM modes. In Eqs. (7a)–(7b), subscripts e of  $\mathbf{u}_e$ ,  $\mathbf{a}_e$ , and  $\mathbf{b}_e$  stand for edge. The subscripts N/D indicate Neumann/Dirichlet BCs.  $\mathbf{u}_e = [ u_1 \quad u_2 \quad u_4 \quad u_5 \quad u_7 \quad u_8 ]^T$ , which is the nodal field vector near edge.  $\mathbf{w}_e^{\text{TE}}$  and  $\mathbf{w}_e^{\text{TM}}$  are the weighted coefficient vector to relate  $u_5$  to  $\mathbf{u}_e$  for TE and TM modes. Note that  $\mathbf{w}_e^{\text{TE}}$  and  $\mathbf{w}_e^{\text{TM}}$  are functions of the offset  $d$ .

$$u(\rho, \phi) = \begin{cases} a_0 J_0(\xi\rho) + \sum_{m=1}^M a_m J_m(\xi\rho) \cos(m\phi), & \text{TE} \\ \sum_{m=1}^M b_m J_m(\xi\rho) \sin(m\phi), & \text{TM} \end{cases}, \quad 0 \leq \phi \leq \pi. \quad (6)$$

$$\begin{bmatrix} \mathbf{P}_N \\ \mathbf{F}_N \end{bmatrix} \mathbf{a}_e = \begin{bmatrix} \mathbf{u}_e \\ u_5 \end{bmatrix} \Rightarrow u_5 = \mathbf{w}_e^{\text{TE}} \mathbf{u}_e, \quad \mathbf{w}_e^{\text{TE}} = \mathbf{F}_N \mathbf{P}_N^{-1}. \quad (\text{EGLFE} - \text{TE}) \quad (7a)$$

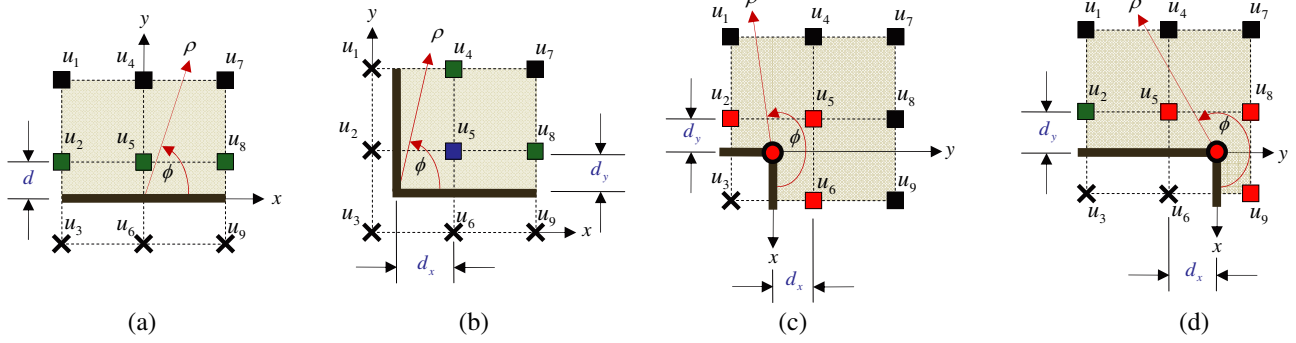


**Figure 3.** Illustration of 9-point stencils near PEC boundaries. (a) Stencil for edge ( $0 < \phi < \pi$ ). (b) Stencil for a regular corner ( $0 < \phi < \pi/2$ ). (c) Stencil for a reentrant corner (Type I with one node removed) ( $0 < \phi < 3\pi/2$ ). (d) Stencil for reentrant corner (Type II with two nodes removed).

$$\mathbf{P}_N = \begin{bmatrix} c_j^i J_j^i \end{bmatrix}, \quad c_j^i J_j^i \triangleq J_j(\xi \rho_i) \cos(j \phi_i), \quad i = 1, 2, 4, 7, 8, \quad j = 0, 1, 2, \dots, M, \quad (7b)$$

$$\mathbf{F}_N = \begin{bmatrix} c_j^5 J_j^5 \end{bmatrix}, \quad \mathbf{a}_e = [a_0 \ a_1 \ a_2 \ \dots \ a_M]^T.$$

$$\begin{bmatrix} \mathbf{P}_D \\ \mathbf{F}_D \end{bmatrix} \mathbf{b}_e = \begin{bmatrix} \mathbf{u}_e \\ u_5 \end{bmatrix} \Rightarrow u_5 = \mathbf{w}_e^{\text{TM}} \mathbf{u}_e, \quad \mathbf{w}_e^{\text{TM}} = \mathbf{F}_D \mathbf{P}_D^{-1}. \quad (\text{EGLFE} - \text{TM}) \quad (8a)$$

$$\mathbf{P}_D = \begin{bmatrix} s_j^i J_j^i \end{bmatrix}, \quad s_j^i J_j^i \triangleq J_j(\xi \rho_i) \sin(j \phi_i), \quad i = 1, 2, 4, 7, 8, \quad j = 1, 2, \dots, M, \quad (8b)$$

$$\mathbf{F}_D = \begin{bmatrix} s_1^5 J_1^5 & s_2^5 J_2^5 & s_3^5 J_3^5 & \dots & s_M^5 J_M^5 \end{bmatrix}, \quad \mathbf{b}_e = [b_1 \ b_2 \ b_3 \ \dots \ b_M]^T.$$

Considering the simplest case that  $t = 0$ , we may simplify Eqs. (7a)–(7b) (EG LFE-TE formulation) as Eq. (9), where  $W_0$ ,  $W_+$ , and  $W_x$  are given by Eq. (5). The coefficients given by Eq. (9) can be equivalently obtained by imposing even symmetry condition (along  $y = 0$ ) on those coefficients defined in Eq. (5) for uniform region.

$$u_5 = W_0^{-1} W_+ (u_2 + 2u_4 + u_8) + W_0^{-1} W_x (2u_1 + 2u_7). \quad (\text{EG LFE-TE for } t = 0) \quad (9)$$

In principle we need all, up to the eighth order, FBS terms to maintain the accuracy of compact coefficients. The local field formulation achieves 8th-order accuracy, and hence FD-discretized Helmholtz equation may enjoy a 6th-order global accuracy (since discretized Helmholtz equation is divided by  $\Delta^2$ ). Once in a while we may use fewer terms to achieve same level of accuracy because of structure symmetries as in the case of the uniform region where we only need FBS terms with orders lower than 5 [5].

### 3.2.1. Local Error Analysis for Edge Grids

Near a PEC edge (denoted as EG) an exact solution of Eq. (1) for the settings given by Fig. 3(a) is expressed as:

$$\psi_{EG}(x, y) = \begin{cases} \cos(qy) e^{-jpx}, & \text{TE} \\ \sin(qy) e^{-jpx}, & \text{TM} \end{cases}, \quad p = \gamma \xi, \text{ and } q = (1 - \gamma^2)^{1/2} \xi. \quad (10)$$

In Eq. (10),  $\gamma$  is defined as the ratio of  $p$  (tangential wavenumber component) to  $\xi$ .  $\psi_{EG}$  is viewed as the superposition of two opposite evanescent waves in  $y$  direction when  $|\gamma| > 1$ . The analytic value of the central field  $u_5^g$  is  $\psi_{EG}$  evaluated at  $x = 0$  and  $y = t\Delta$ . The corresponding numerical value  $u_5^g$  is defined as the weighted sum of  $\psi_{EG}$  evaluated at the coordinates of surrounding nodal fields according to Eq. (4). The weighting factors  $\mathbf{w}_e^{\text{TE}}$  and  $\mathbf{w}_e^{\text{TM}}$  are given by Eqs. (7a)–(7b) and Eqs. (8a)–(8b). The local relative error (LRE) is defined by Eq. (11), which is function of  $\gamma$ ,  $t$ , and the transverse sampling density

$N_\lambda (= 2\pi/V_t)$ . Similar techniques for local error analysis have been proposed in previous researches [12, 13]. Corresponding curves are shown in Figs. 4(a)–4(c) and Figs. 5(a)–5(c).

$$\mathbf{LRE}(N_\lambda, \gamma, t) \triangleq \left| \frac{u_5^n - u_5^a}{u_5^a} \right|. \quad (11)$$

Considering those figures, observations based on LRE analysis are summarized here.

### 3.2.2. I. Offset Effects

We are surprised to learn that LRE is quite sensitive to the normalized offset. The differences between the minimum and maximum LREs are from 2 to 5 orders for both TE cases (Figs. 4(a)–4(b)) and TM cases (Figs. 5(a)–5(b)). For TE cases, the optimized points are near  $t = 0.5$  and  $t = 0$ , but for TM cases, the optimal choices are around  $t = 0.5$  and  $t = 1$ . The convergent rate is about 8th-order when  $t = 0.5$  and lower for other offsets. Hence, the optimal choice of offset may be around half-a-grid spacing.

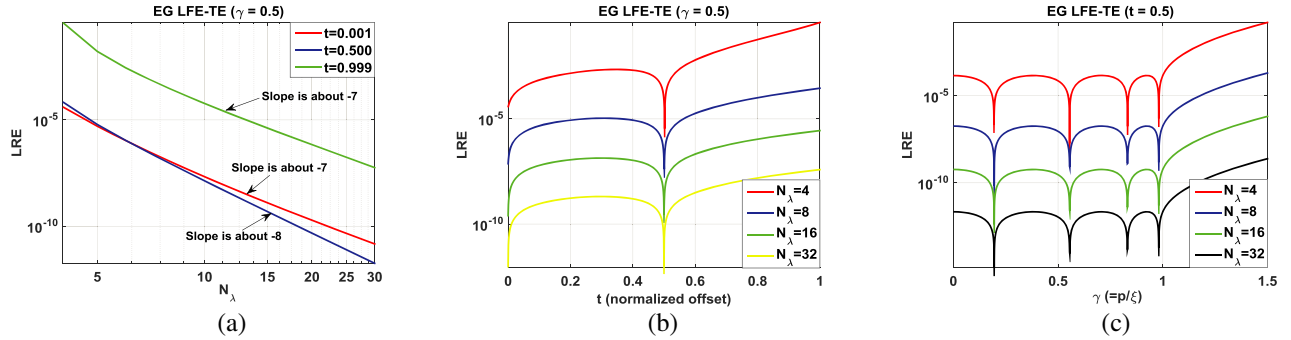


**Figure 4.** Local relative errors (LRE) of edge grids using EG LFE-TE (Eqs. (7a)–(7b)) stencils as functions of (a) transverse sampling density ( $N_\lambda$ ) (b) normalized offset ( $t$ ), and (c) normalized tangential wavenumber ( $\gamma = p/\xi$ ). (Neumann boundary conditions are imposed.).

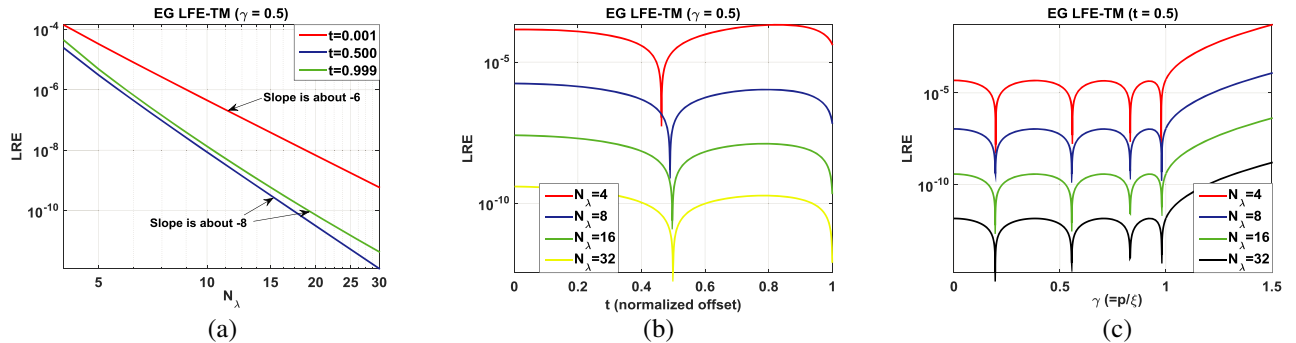


**Figure 5.** Local relative errors (LRE) of edge grids using EG LFE-TM formulation (Eqs. (8a)–(8b)) as functions of (a) transverse sampling density ( $N_\lambda$ ), (b) normalized offset ( $t$ ), and (c) normalized tangential wavenumber ( $\gamma = p/\xi$ ). (Dirichlet boundary conditions are imposed.).

### 3.2.3. II. Angular Spectrum Effects

Effects on spatial angular spectrum dependency are shown in Fig. 4(c) and Fig. 5(c). We see that the overall LREs remain small for propagating plane waves (when  $\gamma < 1$ ) and increase rapidly when  $\gamma > 1$  where the fields are evanescent normal to the PEC surfaces. This may explain why the global mode indices converge with lower order of accuracy when weak singularities fields are presented, hence producing evanescent waves, as will be discussed further in later sections.

### 3.3. Coefficients for Regular Corner ( $\theta_0 = \pi/2$ )

A compact stencil near regular (right-angled) PEC corner is shown in Fig. 3(b). Between the vertex and central node, an offset  $d_x (= t_x \Delta)$  and  $d_y (= t_y \Delta)$  lie in the horizontal and vertical directions. When  $0 \leq t_x < 1$  and  $0 \leq t_y < 1$ , PEC corner coefficients are adjusted for both TM and TE cases. For TE case, when  $t_x = 1$  or  $t_y = 1$ , the situation is reduced to the edge case discussed in Section 3.2. For TM case, if  $t_x = 0$  or  $t_y = 0$ , then the situation can be ignored as the unknowns on the PEC corner/edge are zeros. Local fields near a regular PEC corner (denoted as PEC-CR) are given by:

$$u(\rho, \phi) = \begin{cases} a_0 J_0(\xi\rho) + \sum_{m=1}^M a_{2m} J_{2m}(\xi\rho) \cos(2m\phi), & \text{TE} \\ \sum_{m=1}^M b_{2m} J_{2m}(\xi\rho) \sin(2m\phi), & \text{TM} \end{cases}, \quad 0 \leq \phi \leq \pi/2. \quad (12)$$

Referring to Fig. 3(b) we may obtain the PEC-CR compact coefficients  $\mathbf{w}_c^{\text{TE}}$  and  $\mathbf{w}_c^{\text{TM}}$  with following:

$$\begin{bmatrix} \mathbf{R}_N \\ \mathbf{G}_N \end{bmatrix} \mathbf{a}_c = \begin{bmatrix} \mathbf{u}_c \\ u_5 \end{bmatrix} \Rightarrow u_5 = \mathbf{w}_c^{\text{TE}} \mathbf{u}_c, \quad \mathbf{w}_c^{\text{TE}} = \mathbf{G}_N \mathbf{R}_N^{-1}. \quad (\text{CRLF E} - \text{TE}) \quad (13a)$$

$$\begin{bmatrix} \mathbf{R}_D \\ \mathbf{G}_D \end{bmatrix} \mathbf{b}_c = \begin{bmatrix} \mathbf{u}_c \\ u_5 \end{bmatrix} \Rightarrow u_5 = \mathbf{w}_c^{\text{TM}} \mathbf{u}_c, \quad \mathbf{w}_c^{\text{TM}} = \mathbf{G}_D \mathbf{R}_D^{-1}. \quad (\text{CRLF E} - \text{TM}) \quad (13b)$$

Submatrices are defined in Eq. (14a) and Eq. (14b).

$$\mathbf{R}_N = \begin{bmatrix} c_{2j}^i J_{2j}^i \end{bmatrix}, \quad c_{2j}^i J_{2j}^i \triangleq J_{2j}(\xi\rho_i) \cos(2j\phi_i), \quad i = 4, 7, 8, \quad j = 0, 1, 2, \dots, M, \quad (14a)$$

$$\mathbf{G}_N = \begin{bmatrix} J_0^5 & c_2^5 J_2^5 & c_4^5 J_4^5 & \cdots & c_{2M}^5 J_{2M}^5 \end{bmatrix}, \quad \mathbf{a}_c = \begin{bmatrix} a_0 & a_2 & a_4 & \cdots & a_{2M} \end{bmatrix},$$

$$\mathbf{R}_D = \begin{bmatrix} s_{2j}^i J_{2j}^i \end{bmatrix}, \quad s_{2j}^i J_{2j}^i \triangleq J_{2j}(\xi\rho_i) \sin(2j\phi_i), \quad i = 4, 7, 8, \quad j = 1, 2, \dots, M. \quad (14b)$$

$$\mathbf{G}_D = \begin{bmatrix} s_2^5 J_2^5 & s_4^5 J_4^5 & s_6^5 J_6^5 & \cdots & s_{2M}^5 J_{2M}^5 \end{bmatrix}, \quad \mathbf{b}_c = \begin{bmatrix} b_2 & b_4 & b_6 & \cdots & b_{2M} \end{bmatrix}.$$

#### 3.3.1. Local Error Analysis for Regular Corner

Exact solutions of local field near a PEC-CR (Fig. 3(b)) can be expressed as products of standing plane waves as shown below:

$$\psi_{\text{CR}}(x, y) = \begin{cases} \cos(px) \cos(qy), & \text{TE} \\ \sin(px) \sin(qy), & \text{TM} \end{cases}, \quad p = \gamma\xi, \text{ and } q = (1 - \gamma^2)^{1/2} \xi. \quad (15)$$

The analytic  $u_5^a$  is  $\psi_{\text{CR}}$  evaluated at  $x = t_x \Delta$  and  $y = t_y \Delta$ . Numerical value  $u_5^b$  is just the weighted sum of  $\psi_{\text{CR}}$  evaluated at  $u_4, u_7, u_8$ . The weighting factors  $\mathbf{w}_c^{\text{TE}}$  and  $\mathbf{w}_c^{\text{TM}}$  are given by Eqs. (13a)–(13b). For simplicity, we only consider the case when  $t_x = t_y$ . Computed local relative errors for PEC-CR are presented in Figs. 6(a)–6(c) for the TE cases and in Figs. 7(a)–7(c) for the TM cases. As we can see from Figs. 6–7, local errors behave quite distinctively between the two polarizations. As shown in Fig. 6(c) and in Fig. 7(c), minimum LREs occur when the ratio  $t_y/t_x$  is around 1.

### 3.4. Coefficients for Reentrant Corner

There are two distinct grid layouts near a PEC reentrant corner (denoted as PEC-RC) which are shown in Figs. 3(c)–3(d). For the first type only one nodal field, i.e.,  $u_3$ , is outside the computation domain whereas the second type has two outside nodes  $u_3$  and  $u_6$ . The offset parameters are denoted by  $d_x (= t_x \Delta)$  and  $d_y (= t_y \Delta)$ . When  $t_x = 1$  and  $t_y = 1$ , as illustrated in Fig. 3(c), uniform region coefficients are to be used for  $u_5$ . When  $0 \leq t_x < 1$  and  $0 \leq t_y < 1$ , we must seek adjusted PEC-RC

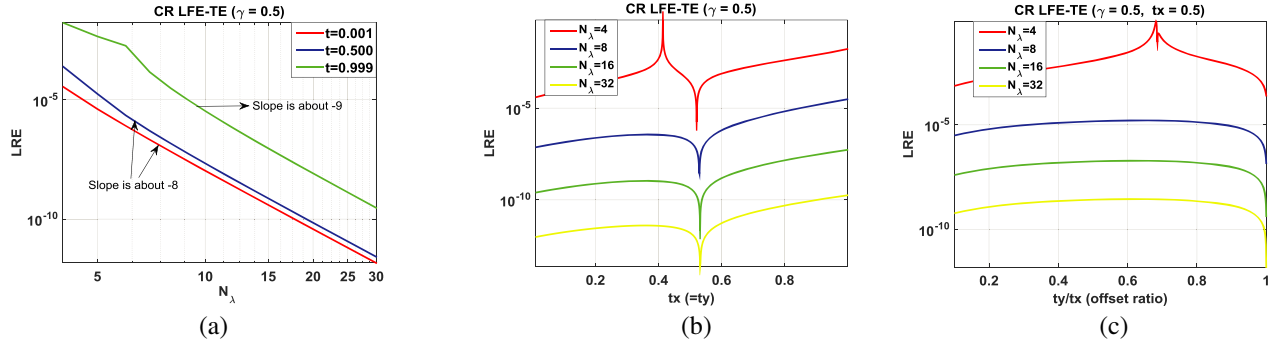


**Figure 6.** Plots of local relative errors (LRE) of CR LFE-TE against (a) transverse sampling density ( $N_\lambda$ ), (b) normalized offset ( $t$ ) and (c) offset ratio ( $t_x/t_y$ ). (Neumann boundary condition).

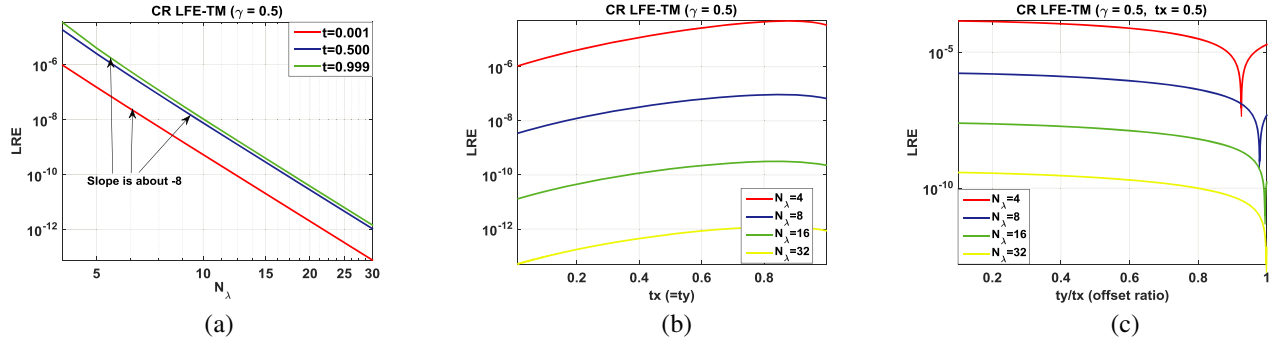


**Figure 7.** Local relative errors (LRE) of CR LFE-TM as functions of (a) transverse sampling density ( $N_\lambda$ ), (b) normalized offset ( $t$ ) and (c) offset ratio ( $t_x/t_y$ ). (Dirichlet boundary condition).

coefficients. Exact FBS-based solutions of the local field near a PEC reentrant corner as illustrated in Figs. 3(c)–3(d), for both TE and TM cases, are given by [9]:

$$u(\rho, \phi) = \begin{cases} a_0 J_0(\xi\rho) + \sum_{m=1}^M a_{2m/3} J_{2m/3}(\xi\rho) \cos(2m\phi/3), & \text{TE} \\ \sum_{m=1}^M b_{2m/3} J_{2m/3}(\xi\rho) \sin(2m\phi/3), & \text{TM} \end{cases}, \quad 0 \leq \phi \leq 3\pi/2. \quad (16)$$

Here PEC-RC compact coefficients  $\mathbf{w}_{\text{RCI}}^{\text{TE}}$ ,  $\mathbf{w}_{\text{RCI}}^{\text{TM}}$ ,  $\mathbf{w}_{\text{RCII}}^{\text{TE}}$  and  $\mathbf{w}_{\text{RCII}}^{\text{TM}}$  are computed by following expressions:

$$\begin{bmatrix} \mathbf{Q}_{\text{N,I}} \\ \mathbf{V}_{\text{N}} \end{bmatrix} \mathbf{a}_{\text{r}} = \begin{bmatrix} \mathbf{u}_{\text{RCI}} \\ u_5 \end{bmatrix} \Rightarrow u_5 = \mathbf{w}_{\text{RCI}}^{\text{TE}} \mathbf{u}_{\text{RCI}}, \quad \mathbf{w}_{\text{RCI}}^{\text{TE}} = \mathbf{V}_{\text{N}} \mathbf{Q}_{\text{N,I}}^{-1}, \quad (\text{RCLFE} - \text{TE} - \text{I}) \quad (17a)$$

$$\begin{bmatrix} \mathbf{Q}_{\text{D,I}} \\ \mathbf{V}_{\text{D}} \end{bmatrix} \mathbf{b}_{\text{r}} = \begin{bmatrix} \mathbf{u}_{\text{RCI}} \\ u_5 \end{bmatrix} \Rightarrow u_5 = \mathbf{w}_{\text{RCI}}^{\text{TM}} \mathbf{u}_{\text{RCI}}, \quad \mathbf{w}_{\text{RCI}}^{\text{TM}} = \mathbf{V}_{\text{N}} \mathbf{Q}_{\text{N,I}}^{-1}, \quad (\text{RCLFE} - \text{TM} - \text{I}) \quad (17b)$$

$$\begin{bmatrix} \mathbf{Q}_{\text{N,II}} \\ \mathbf{V}_{\text{N}} \end{bmatrix} \mathbf{a}_{\text{r}} = \begin{bmatrix} \mathbf{u}_{\text{RCII}} \\ u_5 \end{bmatrix} \Rightarrow u_5 = \mathbf{w}_{\text{RCII}}^{\text{TE}} \mathbf{u}_{\text{RCII}}, \quad \mathbf{w}_{\text{RCII}}^{\text{TE}} = \mathbf{V}_{\text{N}} \mathbf{Q}_{\text{N,II}}^{-1}, \quad (\text{RCLFE} - \text{TE} - \text{II}) \quad (17c)$$

$$\begin{bmatrix} \mathbf{Q}_{\text{D,II}} \\ \mathbf{V}_{\text{D}} \end{bmatrix} \mathbf{b}_{\text{r}} = \begin{bmatrix} \mathbf{u}_{\text{RCII}} \\ u_5 \end{bmatrix} \Rightarrow u_5 = \mathbf{w}_{\text{RCII}}^{\text{TM}} \mathbf{u}_{\text{RCII}}, \quad \mathbf{w}_{\text{RCII}}^{\text{TM}} = \mathbf{V}_{\text{N}} \mathbf{Q}_{\text{N,II}}^{-1}, \quad (\text{RCLFE} - \text{TM} - \text{II}) \quad (17d)$$

where

$$\mathbf{Q}_{N,I} = \left[ c_j^i J_j^i \right], \quad c_j^i \triangleq J_j^i J_j (\xi \rho_i) \cos(j \phi_i), \quad i = 1, 2, 4, 5, 6, 7, 8, \quad j = 0, 1, 2, \dots, M, \quad (18a)$$

$$\mathbf{V}_N = \left[ J_0^5 \quad c_{2/3}^5 J_{2/3}^5 \quad c_{4/3}^5 J_{4/3}^5 \quad \dots \quad c_{2M/3}^5 J_{2M/3}^5 \right], \quad \mathbf{a}_r = [ a_0 \quad a_{2/3} \quad a_{4/3} \quad \dots \quad a_{2M/3} ]^T,$$

$$\mathbf{Q}_{D,I} = \left[ s_j^i J_j^i \right], \quad s_j^i J_j^i \triangleq J_j (\xi \rho_i) \sin(j \phi_i), \quad i = 1, 2, 4, 5, 6, 7, 8, \quad j = 1, 2, \dots, M, \quad (18b)$$

$$\mathbf{V}_D = \left[ s_{2/3}^5 J_{2/3}^5 \quad s_{4/3}^5 J_{4/3}^5 \quad s_2^5 J_2^5 \quad \dots \quad s_{2M/3}^5 J_{2M/3}^5 \right], \quad \mathbf{b}_r = [ b_{2/3} \quad b_{4/3} \quad b_2 \quad \dots \quad b_{2M/3} ]^T.$$

Note that stencil matrices  $\mathbf{Q}_{D,I}$  and matrix  $\mathbf{Q}_{N,I}$  in Eqs. (18a) and (18b) are for PEC-RC type I configuration. Type II PEC-RC matrix  $\mathbf{Q}_{D,II}$  is obtained from  $\mathbf{Q}_{D,I}$  with the last row removed. The same rule applies to  $\mathbf{Q}_{N,II}$ .

### 3.4.1. Local Error Analysis for Reentrant Corner

PEC-EG and PEC-CR structures support (standing) plane wave solutions given by Eq. (10) and Eq. (15), but such solutions do not always exist for PEC-RC shown in Fig. 3(c) and Fig. 3(d). For local error analysis, an exact solution near a PEC-RC,  $\psi_{RC}(x, y)$ , is defined in Eq. (19) by truncating Eq. (16) at the thirtieth term, and all weighting factors are set to be one.

$$\psi_{RC}(\rho, \phi) \triangleq \begin{cases} \sum_{m=0}^{29} J_{2m/3}(\xi \rho) \cos(2m \phi/3), & \text{TE} \\ \sum_{m=1}^{30} J_{2m/3}(\xi \rho) \sin(2m \phi/3), & \text{TM} \end{cases}. \quad (19)$$

The analytic  $u_5^a$  is  $\psi_{RC}$  evaluated at  $x = t_x \Delta$ ,  $y = t_y \Delta$ . Numerical value  $u_5^u$  is just the weighted sum of  $\psi_{RC}$  evaluated at  $u_4$ ,  $u_7$ ,  $u_8$  for Type I-II reentrant corners. For simplicity, we only consider the case when  $t_x = t_y$ . In Figs. 8(a)–8(d) LREs of RC LFE-TM and RC LFE-TE are plotted against transverse sampling density ( $N_\lambda$ ). In Figs. 8(e)–8(h) they are plotted against the normalized offset ( $t_x/t_y$ ). Type II errors are in general somewhat larger, and the orders of convergent rate are less than those of Type I.

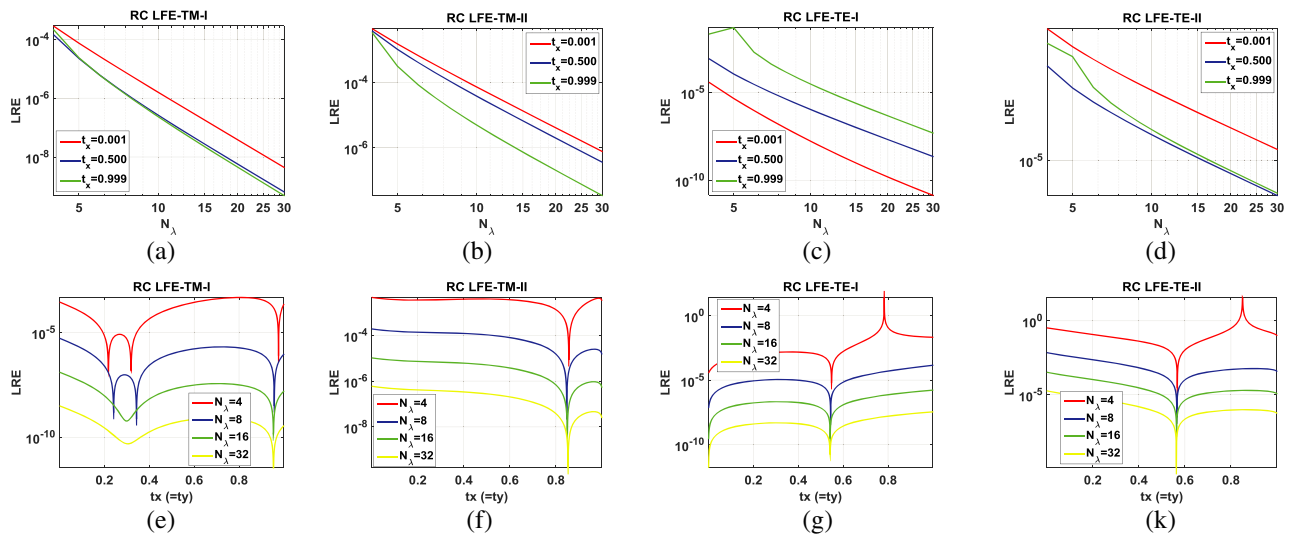


**Figure 8.** Plots of local relative errors of type I and type II of RC-LFE-TM/TE versus transverse sampling density ( $N_\lambda$ ) and normalized offset ( $t_x = t_y$ ).

## 4. NUMERICAL SIMULATION OF MW-WG MODES

### 4.1. Simulation of a Rectangular Waveguide

We now turn to the global error study of our proposed LFE-base compact stencils. First, we look at the rectangular waveguide with a flexible mesh layout as illustrated in Fig. 9. Boundary field points next to the left, right, and top PEC walls are fixed at half-a-grid spacing leaving varying grid spacing at the bottom PEC. The normalized bottom offset is denoted by  $t_B$ . With a fixed waveguide dimension we continuously change the number of sampling points,  $N_x$ , in the  $x$ -direction. Computed global relative errors (RErr) of numerical cutoff frequencies versus  $N_x$  are plotted in Figs. 10(a)–10(c) for  $TE_{10}$ ,  $TE_{01}$ , and  $TE_{11}$  modes. The results for  $TM_{11}$ ,  $TM_{21}$ , and  $TM_{12}$  modes are shown in Figs. 11(a)–11(c). From these plots we see that relative TE mode errors are more sensitive to the normalized bottom offset parameter  $t_B$  than those of TM cases. Overall we observed that the minimum error (with a 6-th order accurate convergent rate) occurs when  $t_B$  equals 0 or 0.5. Convergent rates for the other two cases,  $t_B = 0.25$  and  $t_B = 0.75$ , are only at 5th-order.

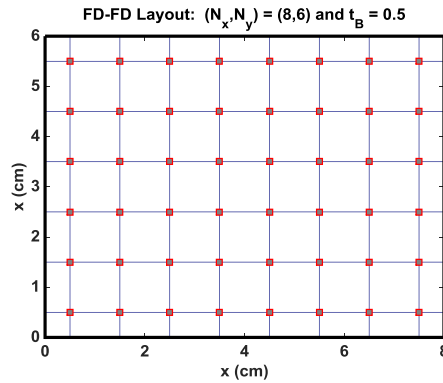


Figure 9. Flexible FD-mesh layout for the rectangular MW-WG.

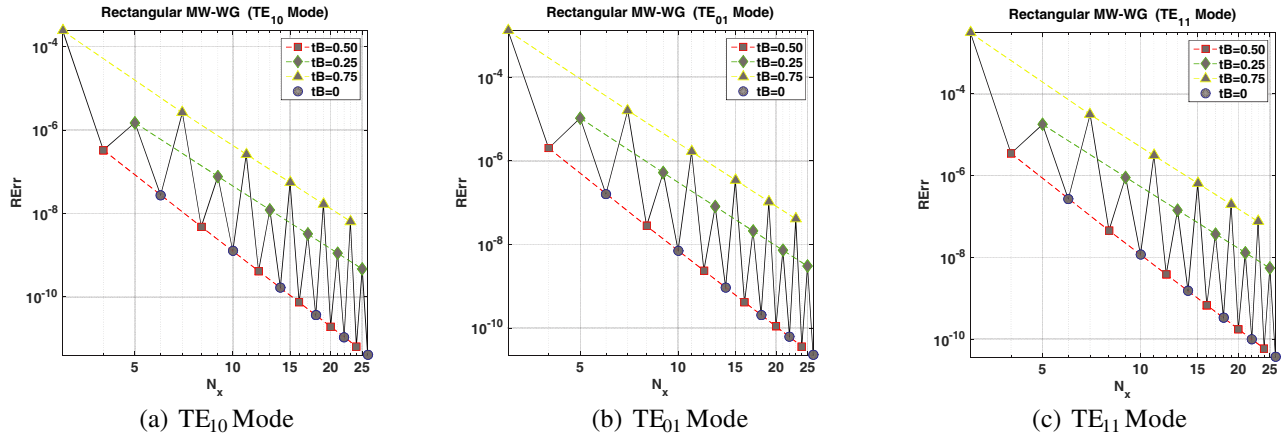
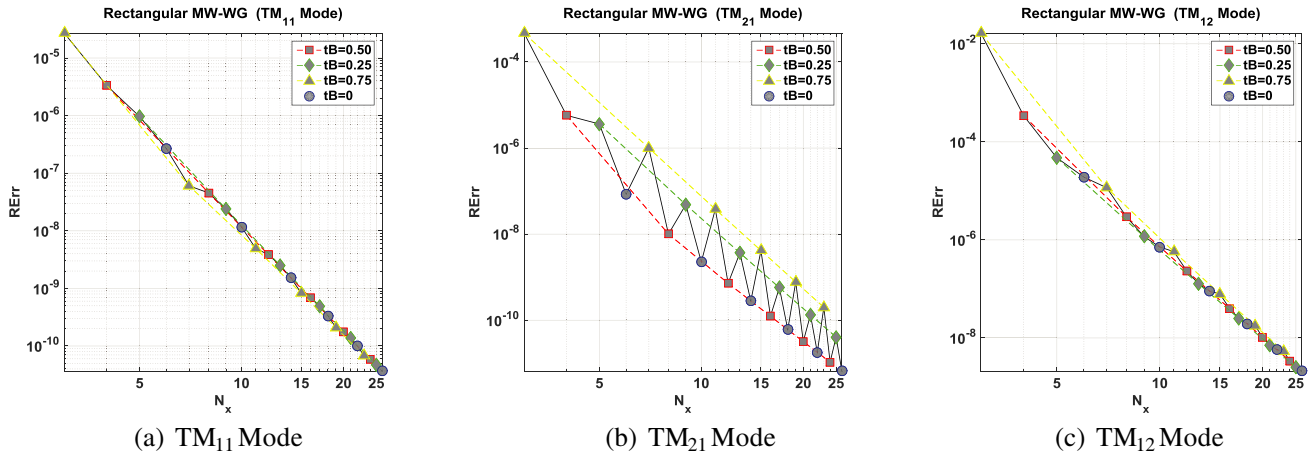


Figure 10. (Rectangular MW-WG) Global relative errors (RErr) of numerical cutoff frequencies for (a)  $TE_{10}$ , (b)  $TE_{01}$ , and (c)  $TE_{11}$  modes as functions of the  $x$ -directional sampling points  $N_x$ .

### 4.2. Simulation of an L-Shaped Waveguide

Finally we test our LFE compact stencils by computing the L-shaped WG made of three unit squares as shown in Fig. 12. In our simulation, the three normalized offsets  $t_L$ ,  $t_{R1}$ , and  $t_{U3}$  are set to be 0.5.



**Figure 11.** (Rectangular MW-WG) Global relative errors of numerical cutoff frequencies for (a)  $TM_{11}$ , (b)  $TM_{21}$ , and (c)  $TM_{12}$  modes as functions of the  $x$ -directional sampling points.

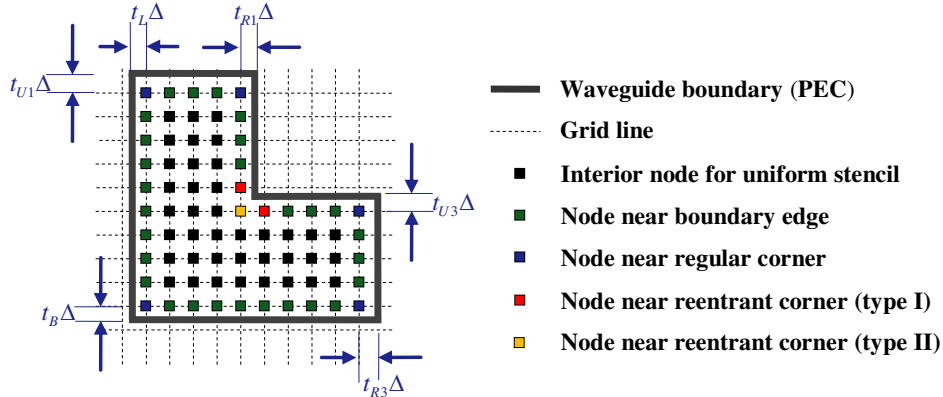


**Figure 12.** Flexible FD-mesh layout for the L-shaped (made of three unit squares) MW-WG. The number of sampling points in  $x$  direction for the upper left square  $N_{x1} = 5$ .

Setting  $L = 1$ , the number of  $x$ -directional sampling points of the upper-left square ( $N_{x1}$ ) is related to the grid spacing  $\Delta$  as  $N_{x1} + t_L + t_{R1} - 1 = L/\Delta$ . Once  $N_{x1}$  is given, the grid size  $\Delta$  and the other three parameters  $t_{U1}$ ,  $t_B$ , and  $t_{R3}$  are determined from it. In Fig. 12, LFE-9 formulation is applied to the nodes marked as black squares. Compact stencils for green and blue nodes are respectively EG LFE stencils (Eqs. (7a)–(7b) and Eqs. (8a)–(8b)) and CR LFE stencils (Eqs. (13a)–(13b) and Eqs. (14a)–(14b)). Stencils for the red and yellow nodes, which are the immediate neighboring grids of the reentrant corner, are adjusted based on Eqs. (17a)–(17d) and Eqs. (18a)–(18b). First ten Dirichlet eigenvalues of Eq. (1) for L-shaped domain can be found in [14], and their square roots serve as the reference values of TM-polarized cutoff frequencies. Later on, a whopping 1001 significant digits of the first Dirichlet eigenvalue for L-shaped domain was given by Jones (2017) [15], where he obtained the result by combing the FHM algorithm [16] with infinite precision floating point arithmetic.

We noted that there were few published eigenvalue results for TE modes of an L-shaped WG. We calculate reference Neumann eigenvalues (not found in previous literatures) using up to 750 thousand unknowns with our in-house band matrix eigenvalue solver. Our LEF-based FD-FD calculations of the first four eigenvalues are listed in Table 2 for TM polarization and in Table 3 for TE polarization. The convergent orders (CO) are still 6 for those modes with analytic eigenfunctions. Global relative errors (RErr) of numerical cutoff frequencies for TE modes and TM modes are shown in Figs. 13. Singularity of higher order modes is weaker than that of the fundamental mode, and hence they have a higher

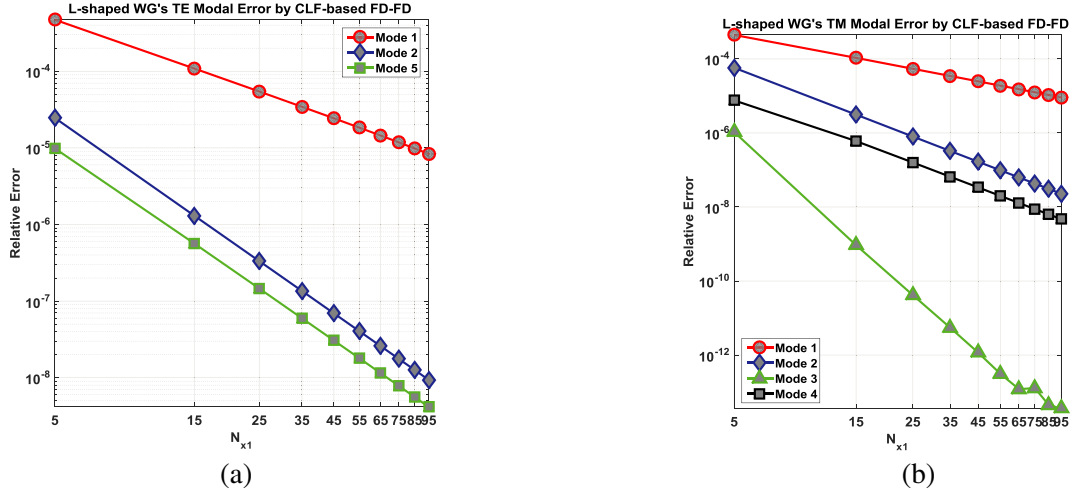


**Figure 13.** (L-shaped MW-WG) Global relative errors (RErr) of numerical cutoff frequencies for (a) TE modes (left) and for (b) TM modes (right).

convergent rate (about 2.7). Resonant transverse wavelengths of higher order modes are shorter than those of lower order modes, so the singularity field of a higher-order mode attenuates much more as it propagates away from the reentrant corner. Thus, the relative errors of higher order modes are smaller than those of lower ones except for analytic cases as listed in Table 2 and Table 3. When  $N_{x1} = 95$  (about 27 thousands variables), our results give 5 significant digits for the fundamental TE/TM modes, and 7 to 8 digits for higher-order singular modes. Nevertheless, the overall convergence orders for the proposed LFE-based FD algorithm are still better than the results reported in [17] where the modified FEM is applied. Since the singularity field spreads out from the reentrant corner, the effect is globalized instead of being localized [7]. This intrinsic limitation impedes numerical performance of solving mode field problems with incoming PEC wedges, or with dielectric corners with high index contrasts, by all FD-FD and FEM algorithms.

**Table 2.** Numerical TM results (DBC) of the L-shaped MW-WG by LFE-based FD-FD solver.

No.	Exact Value of $\xi$ [22]	$\xi (N_{x1} = 95)$	RErr*	CO*	Comments
1	3.1047904	<b>3.10476</b> 20280375	9E-06	1.33	This mode is dominated by $\rho^{2/3}$ term. This is the strongest singular mode.
2	3.8983652	<b>3.898365</b> 3775956	2E-08	2.66	This mode is dominated by $\rho^{4/3}$ term and suffers from less singularity.
3	Exact $\sqrt{2}\pi$	<b>4.442882938158</b> 2	3E-14	6	No singularity. $u(x, y) = A \sin(\pi x) \sin(\pi y)$ .
4	5.4333673	<b>5.433367</b> 4078062	4E-09	2.64	High-order singular mode suffers from less singularity.

\*RErr: relative error; CO: convergent order

**Table 3.** Numerical TE results (NBC) of the L-shaped MW-WG by LFE-based FD-FD solver.

No.	Reference Value of $\xi (N_{x1} = 500)$	$\xi (N_{x1} = 95)$	RErr	CO	Comments
1	<b>1.21475</b>	<b>1.2147</b> 403776183	8E-06	1.33	This mode is dominated by a $\rho^{2/3}$ term and suffers from the strongest singularity.
2	<b>1.8799019</b>	<b>1.8799019</b> 744744	2E-08	2.71	This mode is dominated by a $\rho^{4/3}$ term.
3	Exact $\pi$	<b>3.141592653</b> 9879	1.3E-10	6	No singularity. $u(x, y) = A \cos(\pi x) + B \cos(\pi y)$ .
4	<b>3.374830277</b>	<b>3.374830</b> 2910759	4E-09	2.66	A high-order singular mode converges faster due to a weaker singularity.

## 5. CONCLUSIONS

Traditional FD schemes are limited in two ways. First, the mesh pattern is rectangular and thus is unsuitable for problems with curved boundaries. Second, the accuracy of FD-FD is optimized when square uniform mesh is implemented resulting in arbitrary grid offsets near PEC walls for general waveguide structures. In this paper, we present a flexible LFE-based FD-FD algorithm for simulating complex microwave waveguides with regular and reentrant corners. We maintain the highest possible orders of accuracy for all customized compact stencils near the PEC borders. The cutoff frequency convergence rates for various rectangular waveguides are always 5th- to 6th-order accurate for both types of polarizations.

In the simulation of a typical L-shaped MW-WG, the resonant Neumann frequencies are reported for the first time. We also demonstrate: (a) The local errors of FBSE-based coefficients for these specialized stencils are at least of 5th order; (b) The order of accuracy of the fundamental WG cutoff frequency is one and a third for both the TE mode and TM mode; (c) Numerical results for higher-order singular modes converge faster than those for the fundamental modes; and (d) The convergent rate for analytic modes achieves sixth-order as expected. Compared with the 8-th order accuracy of the uniform cell (local-error), the loss of accuracy for those customized cells near a PEC wall/corner is due to the loss of grid symmetry in the presence nearby PEC boundary. The overall resonant frequencies are not calculated with expected performance of our proposed LFE-based compact stencils. The loss of global accuracy in these cases is entirely due to the singular field emanating from the reentrant corner.

## ACKNOWLEDGMENT

We are grateful for the support of the Ministry of Science and Technology of the Republic of China under the contracts (MOST 107-2221-E-11-045).

## REFERENCES

1. Motz, H., "The treatment of singularities of partial differential equations by relaxation methods," *Quart. Appl. Math.*, Vol. 4, 371–377, 1947.
2. Arfken, G. B. and H. J. Weber, *Mathematical Methods for Physicists*, Elsevier Academic Press, 2005.
3. Antipov, Y. A. and V. V. Sivestrov, "Diffraction of a plane wave by a right-angled penetrable wedge," *Radio Science*, Vol. 42, RS4006, 2007.
4. Hadley, G. R., "High-accuracy finite difference equations for dielectric waveguide analysis I: Uniform regions and dielectric interfaces," *Journal of Lightwave Technology*, Vol. 20, No. 7, 1210–1218, 2002.
5. Chang, H.-W. and S.-Y. Mu, "Semi-analytical solutions of the 2-D homogeneous Helmholtz equation by the method of connected local fields," *Progress In Electromagnetics Research*, Vol. 109, 399–424, 2010.
6. Hadley, G. R., "High-accuracy finite difference equations for dielectric waveguide analysis II: Dielectric corners," *Journal of Lightwave Technology*, Vol. 20, No. 7, 1219–1231, 2002.
7. Magura, S., S. Petropavlovsky, S. Tsynkov, and E. Turkel, "High-order numerical solution of the Helmholtz equation for domains with reentrant corners," *Applied Numerical Mathematics*, Vol. 118, 87–116, 2017.
8. Pozar, D. M., *Microwave Engineering*, John Wiley & Sons, Inc., 2012.
9. Fox, L. and R. Sankar, "Boundary singularities in linear elliptic differential equations," *J. Inst. Math. Applic.*, Vol. 5, 340–350, 1969.
10. Singer, I. and E. Turkel, "High-order finite difference methods for the Helmholtz equation," *Comput. Methods Appl. Mech. Engrg.*, Vol. 163, 343–358, 1998.
11. Nabavi, M. "A new 9-point sixth-order accurate compact finite difference method for the Helmholtz equation," *Journal of Sound and Vibration*, Vol. 307, 972–982, 2007.

12. Mu, S.-Y. and H.-W. Chang, "Theoretical foundation for the method of connected local fields," *Progress In Electromagnetics Research*, Vol. 114, 67–88, 2011.
13. Mu, S.-Y. and H.-W. Chang, "Dispersion and Local-Error Analysis of Compact LFE-27 Formula for Obtaining Sixth-Order Accurate Numerical Solutions of 3D Helmholtz Equation," *Progress In Electromagnetics Research*, Vol. 143, 285–314, 2013.
14. Yuan, Q. and Z. He, "Bounds to eigenvalues of the Laplacian on L-shaped domain by variational methods," *Journal of Computational and Applied Mathematics*, Vol. 233, 1083–1090, 2009.
15. Jones, R. S., "Computing ultra-precise eigenvalues of the Laplacian within polygons," *Advances in Computational Mathematics*, Vol. 43, 1325–1354, 2017.
16. Fox, L., P. Henrici, and C. Moler, "Approximations and bounds for eigenvalues of elliptic operators," *SIAM J. NUMER. ANAL.*, Vol. 4, No. 1, 89–102, 1967.
17. Liu, X.-F. and S. Oishi, "Verified eigenvalue evaluation for the Laplacian over polygonal domains of arbitrary shape," *SIAM J. Numer. Anal.*, Vol. 51, No. 3, 1634–1654, 2013.